RSC Advances

ROYAL SOCIETY OF CHEMISTRY

www.rsc.org/advances

Journal Name

ARTICLE

Graphene-interlayered magnetic composite as a multifunctional SERS substrate

Received 00th January 20xx,
Accepted 00th January 20xx

DOI: 10.1039/x0xx00000x

www.rsc.org/

Jiawen Xu‡[a,b], Chongwen Wang‡[b], Zhen Rong[b], Xiang'ai Cheng[a*] and Rui Xiao[b*]

Investigations of the combination of graphene with noble-metal nanostructures mostly focused on the fabrication of the stacked hybrid film or nanoparticles (Au or Ag NPs) decorated graphene sheets, while few were carried out in graphene built-in monodispersed microspheres. Herein, we proposed a novel hierarchical composite with silver-shelled Fe$_3$ microsphere as the initial core and graphene oxide (GO) as the multifunctional inserted layer. The flexible GO provided abundant nucleation sites for further in-situ growth of Au nanoparticles. Moreover, it introduced considerable chemical enhancement and enhanced surface adsorption toward aromatic molecules. Considering the synergistic properties of versatile GO with noble-metal nanostructures, the synthesized Fe$_3$O$_4$@Ag-rGO-Au microspheres were expected to have excellent surface-enhanced Raman scattering (SERS) activity, which had been verified by the detection of the sulfhydryl-contained PATP and aromatic DTTC with respective detection limit of 10^{-11} M and 10^{-10} M. The enhancement factor (EF) is calculated to be 2.83×10^{6} for totally symmetric (a1) vibrations located at 1077 cm^{-1} of PATP. Additionally, its fast magnetic response enables rapid separation from solution, which is a key factor for many practical applications. Therefore, the well-dispersed hybrid microspheres should have an enormous potential in sensing applications as well as in effective immobilization and enrichment of biomolecules and aromatic pollution.

Introduction

Due to the innate combination of high sensitivity and informative characteristic spectra, surface-enhanced Raman scattering (SERS) deserves tremendous attention in the identification and detection of chemical production, as well as in biochemistry and environment monitoring[1-6]. The crux of exploiting its advantages adequately lies in fabricating high performance SERS substrates[1]. To date, various SERS-active substrates with high Raman enhancement factor (EF) have been successively proposed through proper combination of various noble metal materials (commonly Ag, Au or Cu) and well-designed complex structures either with roughened surface or embedded nanogaps. The periodic nanostructure[7, 8] can achieve well sensitivity and high reproducibility, but has the disadvantage of high cost and being difficult to be further chemically modified. Alternatively, aqueous phase nanostructures are more efficient with flexible control over individual geometry, which are reflected in proposed nanostructures, such as various kinds of gold/silver colloid[9, 10], Au/Ag core-shell structure[11], shell-isolated nanoparticle with adjustable thickness of silica or alumina shell[12], DNA-tailorable nanoparticle with 1-nm interior gap[13] and self-assembled chains of nanorods[14]. Through adjusting the morphology and materials, the predominant electromagnetic enhancement (EM)[15] has been investigated sufficiently, which is believed to contribute to a factor up to 10^{10}. Moreover, controllable fabrication of the predominant nanogaps (hotspots) is extremely challenging[16, 17]. Therefore, additional chemical enhancement must be invoked to release its potential ability for fabrication of multifunctional and effective SERS substrates.

By the virtue of its unique 2D hexagonal carbon structure and accompanied unparalleled physical/chemical properties, graphene[18, 19] finds its role in enormous fields from chemical sensors to electronic devices, and could also be competent in fabricating efficient and biocompatible SERS-active substrates[20]. Graphene oxide (GO), with abundant oxygen-containing functional groups decorated on its surface and the unchanged basic carbon framework, is most promising. The following distinctive structural features and properties provide it with advantages for SERS. Fundamentally, the large flexible surface of GO possesses abundant reactive groups (e.g., carboxyl and hydroxyl) as active sites for facile modification. Besides, it has high adsorption capacity toward various compounds (aromatic species especially) through strong π-π interaction and electrostatic interactions[21, 22]. Furthermore, GO could interact with adsorbed molecules[23, 24] through electron coupling and fast charge transfer, inducing outstanding chemical enhancement and fluorescence quenching effect[25, 26]. Previously reported plasmonic

---

[a.] Address here.
[b.] Address here.
[c.] Address here.
† Footnotes relating to the title and/or authors should appear here.
Electronic Supplementary Information (ESI) available: [details of any supplementary information available should be included here]. See DOI: 10.1039/x0xx00000x

nanoparticle/GO hybrid materials are mainly prepared by in-situ reduction method[27] or encapsulation of GO on as-prepared nanostructures[28-30]. The GO-veiled method enables sufficient utilization of metallic nanostructures with advantages of significant electromagnetic enhancement (EM), chemical enhancement and molecular affinity. Some attempts have been made[31]. However, these composites need to be separated by complex methods, and the experimental configuration still needs optimization.

Magnetic nanoparticles have been extensively investigated for various applications such as drug delivery, magnetic resonance imaging, biosensing and bioanalysis. Due to their superparamagnetic nature[29], Fe_3O_4 microspheres can assist in convenient recycling of novel metals, magnetic enrichment of analytes and rapid separation from reaction system. Therefore, they were often used to form multifunctional composites in combination with other materials. A commonly adopted structure is silver-shelled Fe_3O_4 composite (Fe_3O_4@Ag), which has been widely used in efficient SERS detection or trace analysis[32, 33]. It is fundamental that the synthesized magnetic microspheres should possess high magnetic susceptibility and complete loss of magnetism after removal of external magnetic field. However, extra additives usually lead to the weakening of magnetic susceptibility, and irregular agglomeration easily occurs during shell coating process. Therefore, more efforts should be made to acquire well-dispersed superparamagnetic magnetic composites for better applicability in many different areas.

Herein, we proposed a well-dispersed rGO-interlayered hierarchical magnetic composite, combining effective intraparticle plasmonic coupling with considerable chemical enhancement and additional enrichment properties, which were inherited from the metallic core-shell structure, versatile GO interlayer and magnetic core, respectively. As illustrated in Fig. 1, Fe3O4@Ag-rGO@Au microspheres were synthesized by three steps: superparamagnetic Fe3O4 cores were prepared by the solvothermal reaction; then an Ag shell was assembled upon the core by Au seeds-assisted method. Afterwards, the Fe3O4@Ag microspheres were wrapped with GO nanosheets through electrostatic adsorption. Specifically, large GO sheets were broken into smaller pieces by vigorous sonication for matching with the core-shell microspheres and acquiring full-scale encapsulation. Finally, Au NPs were in-situ grew on the surface with GO converted to reduced GO (rGO) simultaneously. Notably, mechanical stirring and ultrasonication were both employed for sufficient reaction and avoiding aggregation. The SERS performance was evaluated by detecting a standard Raman probe PATP with strong metallic affinity and further estimated by aromatic dye DTTC with continuous-wave laser excitation at a wavelength of 785 nm.

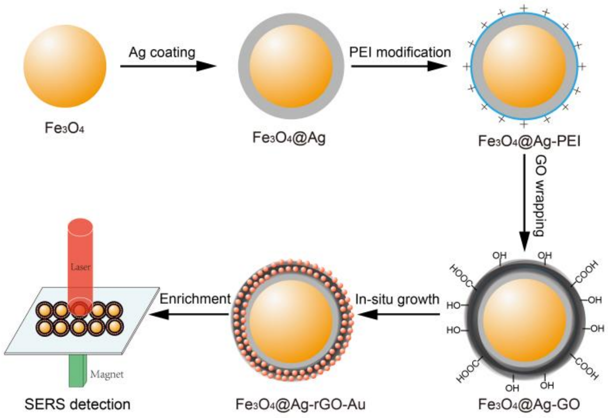

Fig. 1 Schematic illustration of the fabrication process of Fe_3O_4@Ag-rGO@Au microspheres.

Experimental

Synthetic procedures

Synthesis of Fe_3O_4 microspheres

Fe_3O_4 was synthesized by a solvent-thermal method as reported[34]. $FeCl_3·6H_2O$ (1.68 g) was thoroughly dissolved in ethylene glycol (50 mL) then NaAc (4.4 g) and PEG6000 (1.25 g) were added under magnetic stirring. Subsequently, the mixture was transferred into a Teflon-lined autoclave and heated at 200°C for 10 h. The products were collected assisted by external magnet and thoroughly washed with deionized water and ethanol for three times each, and finally dried under vacuum at 60°C for 6 h.

Synthesis of Fe_3O_4@Ag microspheres

Fe_3O_4 microspheres were positively modified with PEI based on its intrinsic self-assembly. 0.25 g PEI was fully dissolved in 50 mL deionized water by ultrasonication. Then 30 mg Fe_3O_4 were added under continuous sonication for 2 h. The produced Fe_3O_4@PEI microspheres were magnetically separated and rinsed for at least five times with deionized water to remove excess polymer. Separately, 3 nm Au nanoparticles were prepared according to previous report the Youxing Fang' method in the previous report[35]. Briefly, freshly prepared $NaBH_4$ solution was rapidly injected into aqueous solution of $HAuCl_4$ and trisodium citrate (Na_3Ct) under vigorous stirring at room temperature. The quick colour change from pale gold to pink indicated the successful formation of 3 nm Au nanoparticles. Finally, the mixture of PEI-modified Fe_3O_4 microspheres and colloidal 3 nm Au NPs was treated by ultrasonication for 1 h to form Fe_3O_4@PEI-Au NPs. Repetitive magnetic separation and thorough rinse were proceeded similarly. The synthesized Fe_3O_4@PEI-Au NPs microspheres were dispersed in 200 mL 0.25 mM silver nitrate aqueous solution containing 0.2 wt% PVP, then excessive formaldehyde (37%, >150 μl) and ammonia (300 μl) were added successively under constant ultrasonication. Fe_3O_4@Ag core-shell microspheres were obtained in a few minutes and were washed repeatedly with deionized water for complete remove of excess PVP, assisted by a magnet for rapid separation.

Preparation of GO nanosheets (nGO) Solution

The bought GO solution (2 mg/mL) possesses a wide size distribution (100nm ~ 1μm) which is too large for the encapsulation of individual microsphere. To obtain GO nanosheets (< 200 nm), 10 mL GO solution was treated with ultrasonication (200 W, 3 h) and then separated by ultracentrifugation (12000 rpm, 30 min). The supernatant (yield ~30%) was extracted as the final product (nGO). The UV absorbance at 230 nm was 0.46 of its 5 × dilution (Fig. S1). The sediment was redispersed in 10 mL of water for recycling.

Synthesis of Fe_3O_4@Ag-rGO-Au composite microspheres

GO-wrapped NPs[36, 37] reported in some reports were synthesized through co-assembly of GO nanosheets with positively charged oxide NPs or amino-functional silica-coated NPs utilizing 3-aminopropyltriethoxysilane (APTES)[38, 39]. However, the prerequisite SiO_2 layer is too thick to form effective nanogaps. In this study, a cocondensation method using PEI was investigated systematacially.

Fe_3O_4@Ag microspheres were positively modified again by PEI in the same way. Afterwards, the amino-modified Fe_3O_4@Ag microspheres were resuspended in excess nGO solution (10 mL) and treated by ultrasonication for 1.5 h, followed by thorough washing with ultrapure water. In an optimized process, the achieved nGO-veiled microspheres were added to a 25 mL three-neck round-bottom flask filled with 15 mL water, then injected 0.9 mL $HAuCl_4$ solution (1%) into the mixture. The mixture was treated by ultrasonication for 30 min for adequate absorption of Au^{3+} on nGO sheets. Afterwards, 1% Na_3Ct (0.6 mL) was added into the mixture dropwise. The reaction was carried at 85°C under continuous mechanical stirring for 1 h, which was adjusted from an aqueous-chemical method[40]. The final Fe_3O_4@Ag-rGO-Au product was separated and collected under external magnet, and then washed for 6 times with ultrapure water and dried in vacuum at 60 °C for 6 h.

Optimization of Fe_3O_4@Ag-rGO-Au nanostructure

To optimize the morphology of in-situ grown Au NPs, three groups of Fe_3O_4@Ag-rGO-Au microspheres were prepared with different amounts of $HAuCl_4$ and Na_3Ct. Meanwhile, all other parameters were maintained the same. For a typical 15 mL system containing 10 mg Fe_3O_4@Ag-GO microspheres, the added amounts of $HAuCl_4$ and Na_3Ct were (a) 0.2 mL and 0.15 mL, (b) 0.9 mL and 0.6 mL, (c) 1.2 mL and 1 mL, respectively. The achieved Fe_3O_4@Ag-rGO-Au microspheres were separately redispersed in 2 mL water for subsequent SERS examinations.

SERS property of Fe_3O_4@Ag-rGO-Au nanostructure

To assess relevant SERS activity, detection of widely recognized probe molecule, sulfhydryl-contained PATP, and aromatic DTTC were conducted. PATP alcoholic solution with a concentration of 10^{-7} M was applied in the examination of the specific contribution of different additives to final SERS signals, as well as in the comparison of the SERS performance of Fe_3O_4@Ag-rGO-Au microspheres (5 mg/mL) synthesized with different amounts of $HAuCl_4$ and Na_3Ct. For the determination of the SERS sensitivity of the optimized nanostructure, a series of PATP alcoholic solutions with variable concentration ranging from 10^{-7} to 10^{-12} M were prepared accurately. The procedure steps were the same for different detections. Each tube of freshly prepared PATP solution (2 mL) was mixed with 2 μl of as-prepared microspheres dispersion (5 mg/mL), and the mixture was mildly sonicated for 0.5 h, therefore allowing adequate molecular adhesion. Afterwards, the samples were concentrated and dropped onto Si substrates which were cleaned thoroughly with water and alcohol beforehand. Few minutes later after complete evaporation of the solvent, SERS signals were recorded. Power at samples was 20% of the full laser power and the integration time was 10 s. Similarly, a series of DTTC aqueous solutions were prepared with concentration ranging from 10^{-6} M to 10^{-11} M for the examination of SERS sensitivity to aromatic molecules. And DTTC solution with concentration of 10^{-7} M was precisely prepared for comparison with Fe_3O_4@Ag. Raman spectra were collected under same procedure except decreasing the integration time to 5 s.

Materials

Silver nitrate, Ferric chloride (Fe_3O_4•$6H_2O$), Ethylene glycol, formaldehyde (37%), ammonia (28%), chloroauric acid tetrahydrate ($AuCl_3$•HCl•$4H_2O$) were purchased from Sinopharm Chemical Reagent Co. Poly(ethyleneimine) (PEI, MW 25000), Polyvinylpyrolidone (PVP, MW 40000), p-aminothiophenol (PATP) and 3,3'-diethylthiatricarbocyanine iodide (DTTC) were purchased from Sigma–Aldrich Chemicals Co. Graphene oxide solution (2mg/mL) was purchased from Nanjing XFNANO Materials Tech Co. The other chemicals were supplied by Shanghai Chemical Reagent Co. Specifically, all chemicals were of analytical grade. Ultrapure water for all solution preparation was produced with Milli-Q system (18.2 MΩ cm^{-1}).

Instruments

Scanning electron microscope (SEM) images were taken using a JEOL JSM-7001F microscopy operated at 5 kV equipped with an energy dispersive X-ray (EDX) analyser; Transmission electron microscope (TEM) images and High resolution TEM images were taken on a Hitachi H-7650 TEM and JEOL-2010 HRTEM at an accelerating voltage of 200 kV, respectively. The specimens were prepared by drop casting the sample dispersion onto a carbon-coated copper grid, and then being dried under room temperature. Zeta potential measurements were performed in a Brookhaven Zeta PALS instrument. The crystalline structure was investigated by X-ray power diffraction (RIGAK, D/MAX 2550 VB/PC, Japan). The magnetic properties of the products were investigated by using a superconducting quantum interference device magnetometer (SQUID, MPMSXL-7) at 300K. X-ray photoelectron spectroscopic (XPS) measurements were carried out on a Thermo ESCALAB 250X, America, equipped with a hemispherical electron analyser and an Al Kα X-ray radiation source (150 W, hv=1486.6 eV), with an energy step size of 1 eV and a pass energy of 1361 eV. Raman spectra was recorded with a portable Raman system (B&W Tek, i-Raman Plus BWS465-785H spectrometer) under 785 nm laser excitation, whose power at excitation port was 340 mW. A 20× microscope objective was applied to precisely focus the laser beam with a spot size of 105μm. Besides, the back-illuminated CCD cooled at -2 °C was used as the detector.

Results and discussion

The Characterization of Fe_3O_4@Ag-rGO-Au Nanostructure

The hierarchical Fe_3O_4@Ag-rGO-Au microspheres were successfully prepared according to the synthesis route illustrated in Fig. 1. All microspheres possess expected size, morphology and surface modification as confirmed by TEM and SEM images (Fig. 2 a-k). Fe_3O_4particles were synthesized stably through solvothermal reaction with a diameter of 400nm (Fig. 2 a). In the following step, Fe_3O_4 particles were amino-modified with PEI, which brought in dual benefits of dense adhesion of 3 nm Au NPs on the surface and avoiding agglomeration due to the introduced excellent hydrophilic properties. The adsorbed tiny Au NPs served as nucleation sites (Fig. 2 b) and assisted in fabrication of compact and uniform Ag shell (50 nm in thickness) with subtle roughness as presented in Fig. 2 c and d, revealing their positive role as seeds in facilitating growth of silver nanoparticles precursor and eventual compact and uniform silver coating. Additionally, the synthesized microspheres were well separated from each other and had an extreme narrow distribution in size. After PEI-modification, the positively charged core-shell Fe_3O_4@Ag microspheres reacted with negatively charged nGO solution and were fully wrapped with nGO sheets as displayed in Fig. 2 e, f. The corresponding HRTEM image (Fig. 3 a) shows an enlarged feature of the wrapped GO nanosheets, characterized by the expanded nearly transparent wrinkles. Additional evidence was provided by Zeta potential measurement, in which the ζ-potential decreases obviously from +39.6 mV to −1.5 mV, hinting that negatively charged GO nanosheets were tightly adsorbed onto the surface through the electrostatic force and encapsulated the Ag shell from ambient environment. Simultaneously, the GO nanosheets served as structural supporting for densely growth of Au nanoparticles (Au NPs) through in-situ reduction process and formed the outmost layer of the composite. However, as observed in Fig. 3 b and c, the morphology of Au NPs was deteriorated unavoidably[36, 37, 41] due to the interference of the unique structure of GO. Meanwhile, the density and size distribution of formed Au NPs were easily influenced by the amounts of $HAuCl_4$ and sodium citrate. To analyze the relationship between amounts of reagents and morphology of Au NPs, three groups of Fe_3O_4@Ag-rGO-Au microspheres were synthesized in the ways as described in experimental section. As illustrated in Fig. 3 d-f, it is apparent that the increase of $HAuCl_4$ amount leads to increased density of Au NPs at first. However, excessive Au^{3+} ions reversely give rise to large nonspherical Au NPs and are more likely to induce agglomeration. A reasonable explanation is that merely a limited number of Au NPs could be formed restricted by the finite number of active sites on GO nanosheets. After reached the saturation point, redundant Au^{3+} ions were rapidly reduced and nucleated in solution during the initial process[40]. And the following coalescence process provided adequate opportunities for them to attach with those formed on GO nanosheets, and to further grow into large-size irregular nanoparticles.

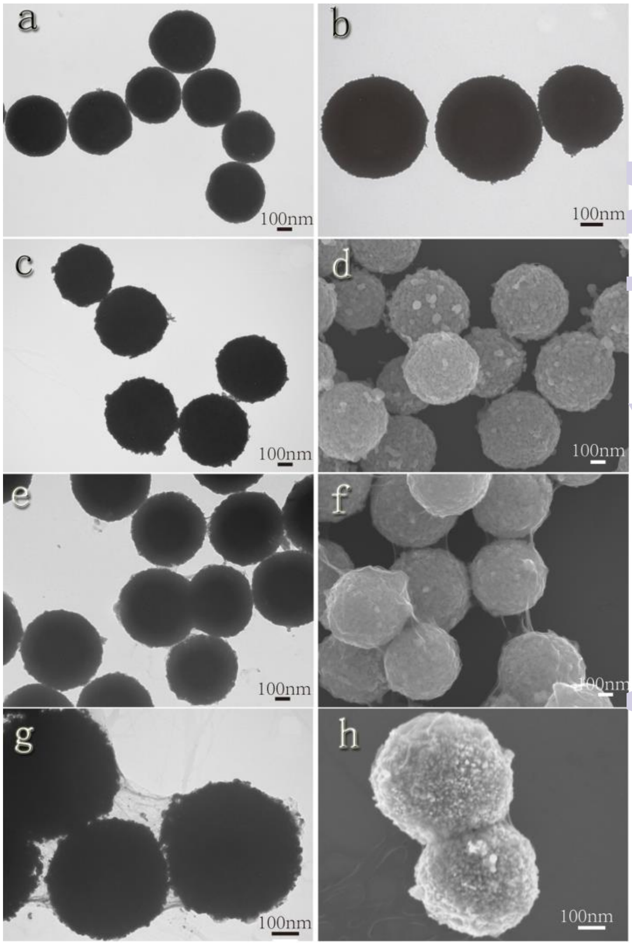

Fig. 2 TEM images of (a) Fe_3O_4 microspheres (b) Fe_3O_4@3nm Au NPs, (c, d) Fe_3O_4@Ag microspheres (e, f) Fe_3O_4@Ag-GO microspheres, (g, h) Fe_3O_4@Ag-rGO-Au microspheres, respectively.

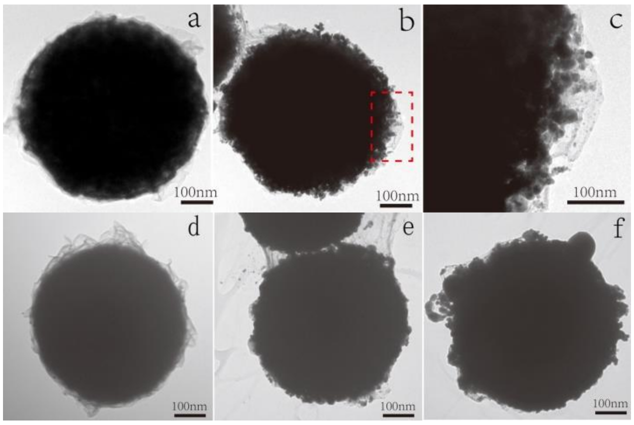

Fig. 3 HRTEM images of (a) Fe_3O_4@Ag-GO microspheres and (b) Fe_3O_4@Ag-rGO-Au microspheres and its enlarged HETEM images(c). TEM images of Fe_3O_4@Ag-rGO-Au microspheres formed with different amounts of $HAuCl_4$ and Na_3Ct: (d) 0.2 mL $HAuCl_4$ and 0.15 mL Na_3Ct; (e) 0.9 mL $HAuCl_4$ and 0.6 mL Na_3Ct; (f) 1.5 mL $HAuCl_4$ and 1 mL Na_3Ct.

To characterize the formation of nanocrystals and their crystalline properties, wide-angle powder X-ray diffraction (XRD) measurements were performed as shown in Fig. 4. The face-centred Fe_3O_4 core shows abundant X-ray diffraction peaks identical to the standard spectrum (JCPDS No.75-1609)[42]. Specifically, six dominate peaks at 30.1°, 35.44°, 43.1°, 53.4°, 57.2° and 62.6° are labeled, which are assigned to planes (112), (211), (220), (024), (303), and (224), respectively. As to the Fe_3O_4@Ag composite, four new intense peaks appearing at 38.2°, 44.3°, 64.5° and 77.5° are ascribed to the (111),(200), (220) and (311) lattice planes of the face-centered cubic (fcc) phase of Ag (JCPDF No. 4-0783). Accordingly, the intensities of all peaks of Fe_3O_4 are significantly weakened due to the compact Ag shell. Nevertheless, the survey spectrum of Fe_3O_4@Ag-GO microspheres seems the same with that of Fe_3O_4@Ag microspheres. For validation of the result, different groups of samples were measured independently and all groups leaded to the same result. It is suggested that the marginal content of nearly transparent GO produces negligible loss of signals. As to the pattern for Fe_3O_4@Ag-rGO-Au composite, it shows no position change of characteristic peaks except a moderate increment of intensity when compared to Fe_3O_4@Ag-GO, since Au shares particularly close characteristic peaks with Ag.

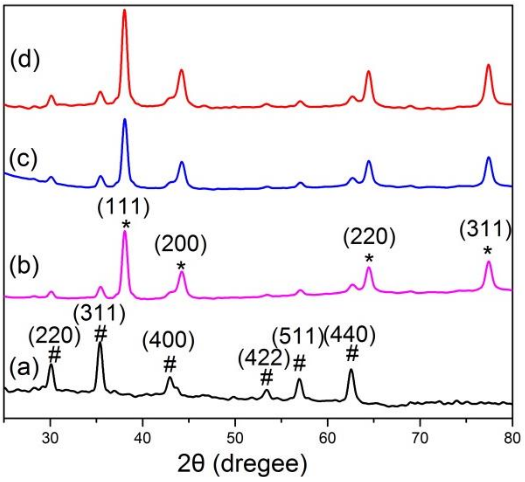

Fig. 4 Wide-angle XRD patterns of (a) Fe_3O_4 microspheres (characteristic peaks of Fe_3O_4 were marked with '#'), (b) Fe_3O_4@Ag microspheres (characteristic peaks of Ag were marked with '*'), (c) Fe_3O_4@Ag-GO microspheres and (d) Fe_3O_4@Ag-rGO-Au microspheres, respectively.

To further confirm the elemental compositions and corresponding chemical states, X-ray photoelectron spectroscopy (XPS) analyses were conducted. As shown in Fig. S2, a distinct Au4f doublet peak arises in XPS survey spectrum of Fe_3O_4@Ag-rGO-Au and the O1s peaks decrease when compared with Fe_3O_4@Ag-GO, indicating the successful formation of Au NPs and simultaneous reduction of GO in final step. The high-resolution of C1s XPS spectra in Fig. 5a and b consist of three fitting peaks, corresponding to sp^2 and sp^3 C (284.6 eV), C-O (286.5 eV) and C=O (288.7 eV), respectively. Specifically, the increased integrated area of sp^2 C and the decreased oxygenated carbon moiety content consistently validate the effective removal of oxygen functional groups from GO nanosheets (termed as GO-to-rGO conversion) by nucleophilic substitution with Au^{3+}. Fig. 5c displays the Ag3d doublet peaks at 367.6 eV (Ag 3d5/2) and 373.6 eV (Ag 3d3/2) with a value difference of 6.0 eV, suggesting composition of Ag0. Similarly, the value difference (3.7 eV) between Au 4f7/2 and Au 4f5/2 suggests the metallic state of Au, and its percentage is calculated almost 100% from the Au4f XPS spectra (Fig. 5d). A slight shift to higher binding energy (0.2 eV) is observed as well. A reasonable explanation is that the work function of Au is lower than that of rGO (>4.8eV, depending on the amount of oxygen functionalities[26]), resulting in fast charge transfer from GO to Au NPs.

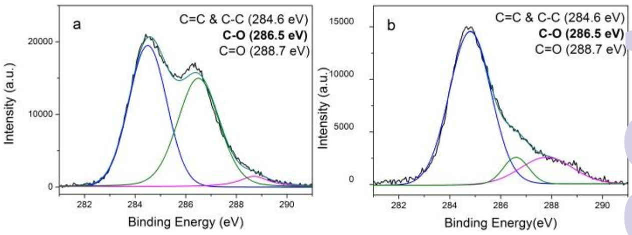

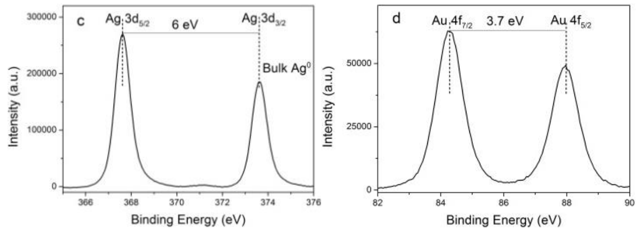

Fig. 5. XPS spectra of (a) C 1s from Fe_3O_4@Ag-GO microspheres and C 1s (b), Ag (c), Au (d) from Fe_3O_4@Ag-rGO-Au microspheres.

Fig. 6 displays hysteresis loops investigated by superconducting quantum interference device (SQUID) magnetometer at 298 K. Obviously, the perfect zero coercivity and reversible hysteresis behaviors demonstrate the excellent superparamagnetic nature of all synthesized composites, which is inherited from the Fe_3O_4 cores. The additive of a new layer decreases the saturated magnetization value from initial 86.1 emu g-1 to final 51.4 emu g-1, but the value is still much higher than that of previously formed magnetic composite[43]. The well-maintained superparamagnetic nature guarantees convenient manipulation and total loss of magnetism after external magnetic field is withdrawn, which prevents from unwilling aggregation during fabrication process due to residual magnetism.

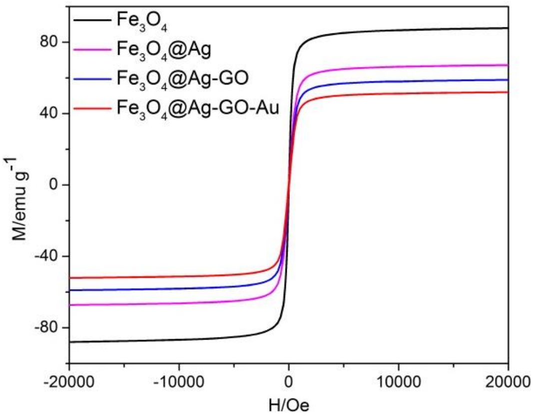

Fig. 6 Hysteresis loops of Fe_3O_4@Ag, Fe_3O_4@Ag-GO, and Fe_3O_4@Ag-rGO-Au composites.

SERS properties of the Fe_3O_4@Ag-rGO-Au structure:

With sufficient hotspots and adequate exposed surface of rGO, the well-dispersed Fe_3O_4@Ag-rGO-Au composite is expected to have brilliant SERS performance. Besides, the additional superparamagnetic nature could considerably enable further improvement on detection sensitivity, which originated from the magnetism-induced aggregation and enrichment of targeted analytes, and endows the microspheres with practical application such as food detection and environment monitoring. The SERS activity and adsorbability were evaluated using sulfhydryl-contained PATP and sulfhydryl-absented DTTC as absorbed target molecules. Both of them have no optical absorption in near-IR region. Therefore, the consequential non-resonance SERS responses were exclusively assigned to the substrate properties.

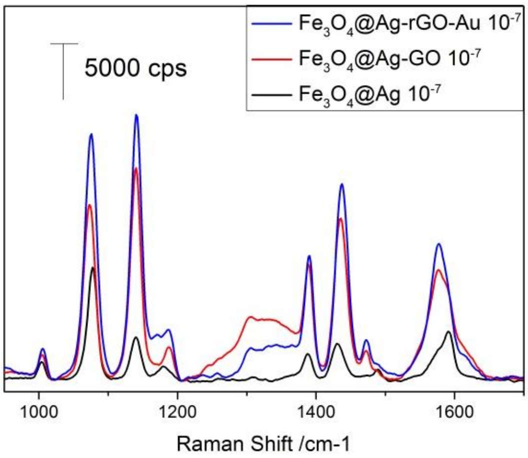

Fig. 7 Comparison of SERS spectra of PATP solution (10-7 M) from different intermediated structures: (A) Fe_3O_4@Ag, Fe_3O_4@Ag-GO and Fe_3O_4@Ag-rGO-Au. The integration times were 10 s and the excitation laser energy was 20% of the full laser power. Each spectrum is the average of five SERS spectra and has undergone baseline subtraction.

To verify the specific contribution of different additive to final SERS signals, a common Raman probe, PATP, was applied for comparison of signal enhancements of different intermediated structures (i.e. Fe_3O_4@Ag, Fe_3O_4@Ag-GO and Fe_3O_4@Ag-rGO-Au). This compound was chosen because of the strong affinity of its mercapto (-SH)[44, 45] end group to Au NPs via Au–S bond and its aromatic ring to highly flat GO nanosheets via π-π interactions, which leads to the spontaneous formation of self-assembled monolayer and could exclude interference factor of the number of absorbed analytes.

As revealed in Fig. 7, distinct Raman peaks of PATP assigned to totally symmetric (a1) vibrations (a1-type, marked with '*', mainly 1077 and 1577 cm-1) and non-totally symmetric (b2) vibrations (b2-type, marked with '#', mainly 1142, 1390 and 1439 cm-1) are observed and are in good agreement with previous reports as categorized in Fig, S3 and Table. S1. The overview of the recorded spectra for different structures indicates that the intensities of all spectral bands monotonously increased, suggesting steadily improved SERS enhancement due to the introduction of GO and Au NPs. Additionally, prominent D and G bands of GO/rGO were easily observed due to strong signal amplification of the beneath Ag shell. To avoid the overwhelming intensity of the carbon bands, few microspheres (2 µl) were added and sparsely spread o SiO2/Si substrates. As seen in the figure above, the low broad peak (between 1200 and 1400 cm-1) of reduced graphene oxide does not disturb the observation of targeted signals. Th a1-type Raman peaks demonstrate that all synthesize structures generate pronounced local field enhancements du to the metallic component, mainly rough Ag shell and dense distributed Au NPs. The b2-type vibrations are highly sensitive to the substrate material and have been regarded as symbo bands associated with chemical enhancement (CM). Therefore, the CM abilities of different materials could be interpreted from the spectra. Specifically, take the main a1 band (1077 cm^{-1}) as reference, the intensity ratio of an intense b2 band (1142 cm^{-1}) to it markedly increases from 0.334 to 1.273 and then encounters a slight decrease to 1.079, suggesting that GO possesses more remarkable CM than silver and gold. It could be illustrated that the π-π interaction of graphene-molecule directly increases the polarizability of PATP as well as the corresponding cross section of the Raman scattering and facilitates faster charge transfer process between PATP and graphene. As to the final structure, GO surface was densely covered by Au NPs and accordingly weakened the CM proportion of GO contributed to the total signal, however, the overall signal was still enhanced, due to the overcompensation of more prominent EM induced by plasmon coupling of interparticles.

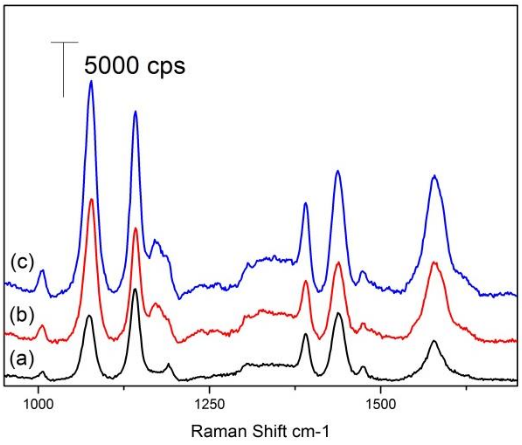

Fig. 8 Comparison of SERS spectra of PATP solution (10^{-7} M) from Fe_3O_4@Ag-rGO-Au microspheres with different synthesized conditions: as previously confirmed by TEM images (Fig.3 d-f), the respective microspheres had (a) the lowest density and smallest size; (b) medium density and largest size but irregular morphology; (c) the highest density and medium size. The spectra were recorded in the same way, and have been offset vertically for visualization.

The SERS performance of Fe_3O_4@Ag-rGO-Au microspheres with different density and size of Au NPs were evaluated with 10^{-7} M PATP alcoholic solution. The recorded spectra are summarized in Fig. 7 B. Raman spectra of group (a) with most few Au NPs are similar to that of Fe_3O_4@Ag-GO microspheres, hinting that the few Au NPs merely produce negligible contribution to overall signal. As to group (b) with irregular Au NPs of medium density, both a1-type and b2-type bands are enhanced, and it should be noted that the a1 band exceeds the b2 band. It could be interpreted that large Au NPs exhibited plasmonic intercoupling with inner Ag shell and neighbour particles, leading to better electromagnetic enhancement and therefore higher a1 bands. The best performed structure is group (c) with relatively uniform size and the highest density. It is suggested that the formation of large size Au NPs results in rapid decrease of the number of effective spots in the vicinities of Au NPs. Besides, the large separation between neighbor Au NPs hinders possible intraparticle coupling, which contributed to signal amplification effectively. Conclusively, the best performed nanostructure was determined and the synthesis parameters were applied in all subsequent experiments.

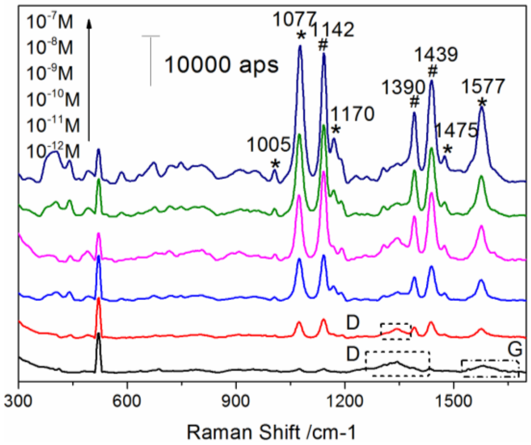

Fig. 9 Raman spectra of PATP with a series of concentrations range from 10^{-7} M to 10^{-12} M. The excitation laser energy was set to 20% of the full laser power with an integration times of 10 s. Each spectrum is the average of five SERS spectra and has undergone baseline subtraction.

To shed more light on the SERS enhancement capacity, a concentration profile experiment illustrating the sensitivity of synthesized structure was conducted. As displayed in Fig. 7b, all characteristic peaks are distinctly recognized even at a low concentration of 10^{-11} M and gradually decrease as the concentration decreases. The characteristic peak of Si located at 520 cm-1 was used as the reference signal to ensure the number of microspheres exposed in the laser spot and other detecting conditions were controlled as the same. At a concentration of 10^{-12} M, the primary Raman peaks can be hardly distinguished and are hidden in the shoulder of the D (1350 cm^{-1}) and G (1580 cm^{-1}) bands of graphene. The SERS enhancement factor (EF) for PATP is roughly estimated referring to an adjusted method described in detail in the supplement information. The EF value[15] of peak at 1077 cm^{-1} is estimated to be about 2.83×106. Considering that the microspheres were far from saturated adsorption, the actual EF value should be higher. The limit of detection (LOD) and EF value are superior to that of other G/GO-hybrid composites and conventional noble metal substrate. The excellent SERS performance reveals that GO nanosheets plays a multi-functional improving role and produces dramatic synergistic effect combined with metallic nanostructures. Typically, GO nanosheets provide strong molecular adsorption, π-π interaction, fast charge transfer process with analytes and therefore noticeable chemical enhancement, all of which contribute collectively to final signals. Besides, the highly transparent GO with atom thickness causes negligible electromagnetic damping of signals, which is usually unavoidable in commonly used SiO_2/Al_2O_3 shell. And this property makes GO an alternative material for a biocompatible protection and structural supporting. In addition, the intrinsic nucleation sites for growth of nanoparticles on its large surface refrain from multiple polymer modification.

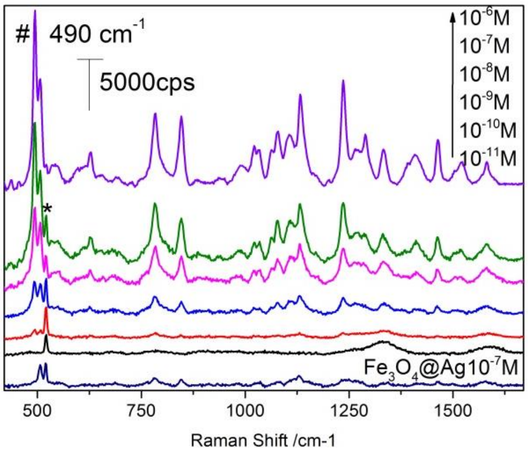

Fig. 10 Raman spectra of DTTC with a series of concentrations range from 10^{-6} M to 10^{-11} M. The excitation laser energy was set to 20% of the full laser power. And the integration times were 10 s to spectra of 10^{-11} M and 5 s to all other groups. The spectra have been offset vertically for visualization.

The capacity of monitoring aromatic compounds was demonstrated by detection of sulfhydryl-absented DTTC, a positively charged infrared dye. A series of DTTC solutions ranging from 10^{-6} M to 10^{-11} M were detected following similar procedure except that the integration times was reduced to 5 s in case of photobleaching. The Raman spectra of DTTC match well with previous report[46], and all characteristic peaks could be clearly identified even at a low concentration of 1 nM. When the solutions were further diluted to 0.1 nM, the primary peak located at 490 cm-1 (marked with '#') still could be easily recognized. As shown in the last spectrum of Fig. 8, the signal intensities of DTTC (10^{-7} M) detected by Fe_3O_4@Ag is much lower than that by Fe_3O_4@Ag-rGO-Au. It is obvious that the additive of rGO-Au enhances the SERS sensitivity by two magnitudes and hints that GO nanosheets add new driving force for spontaneous surface adsorption, which is especially important for SERS analyses in colloidal systems. In all above experiments, the excellent superparamagnetic nature of composites greatly facilitates all manipulation and endows rapid detections. Similarly, its counterpart peak assigned to Si remained unchanged, implying that the measurements were performed under the same condition. D and G band of GO/rGO were well controlled at a low level and could be observed only when the integration time was doubled to 10 s.

Conclusions

In conclusion, we have developed a hierarchical magnetic composite with well rationalization of high dispersibility, convenient separability and robust sensitivity, in which graphene oxide (GO) served as an interlayer and played multiple roles in structure fabrication and integral SERS signal enhancement. The remarkable chemical enhancement (CM) mainly generated by GO was reflected in the sharp increment of relative intensity ratio of non-totally symmetric (b2) vibrations to totally symmetric (a1) vibrations of PATP in the Raman spectra of Fe_3O_4@Ag-GO compared to Fe_3O_4@Ag. Additionally, its sensitivity to various analytes preliminary behaves in the low limit of detection of sulfhydryl-contained PATP (10^{-11} M) and aromatic DTTC (10^{-10} M). And the EF is estimated as 2.83×10^{6} for bands of PATP located at 1077 cm^{-1}. This study validates the initial expectation to the Fe_3O_4@Ag-rGO-Au microspheres as efficient SERS substrates and suggests promising potential in spectroscopic identification of diverse analytes and environmental pollutant detection due to the rapid separation and magnetically induced aggregation inherited from the magnetic core. Furthermore, by controlling the size of cracked GO sheets, similarly structured microspheres with various sizes can be easily produced and generate new synergistic effects for biomedical applications such as NIR-sensitive photothermic therapy[47] and biological imaging[48] can be observed.

Acknowledgements

This work was supported by the National Natural Science Foundation of China (No. 31100712).

Notes and references

‡ These authors contributed equally to this work.

1. M. Fan, G. F. Andrade and A. G. Brolo, *Anal Chim Acta*, 2011, **693**, 7-25.
2. S. Nie and S. R. Emory, *Science*, 1997, **275**, 1102-1106.
3. A. Campion and P. Kambhampati, *Chemical Society reviews*, 1998, **27**, 241-250.
4. X. Qian, X. Zhou and S. Nie, *Journal of the American Chemical Society*, 2008, **130**, 14934-14935.
5. Y. C. Cao, R. Jin and C. A. Mirkin, *Science*, 2002, **297**, 1536-1540.
6. S. Zeng, D. Baillargeat, H.-P. Ho and K.-T. Yong, *Chemical Society reviews*, 2014, **43**, 3426-3452.
7. Y. Zhao, X. Li, Y. Du, G. Chen, Y. Qu, J. Jiang and Y. Zhu, *Nanoscale*, 2014, **6**, 11112-11120.
8. W. Xu, J. Xiao, Y. Chen, Y. Chen, X. Ling and J. Zhang, *Advanced Materials*, 2013, **25**, 928-933.
9. P. D. Howes, R. Chandrawati and M. M. Stevens, *Science*, 2014, **346**.
10. M. Rycenga, C. M. Cobley, J. Zeng, W. Li, C. H. Moran, Q.

---

a College of Optoelectronic Science and Engineering, National University of Defense Technology, Changsha 410073, China. E-mail: xiang_ai_cheng@126.com.
b Beijing Institute of Radiation Medicine, Beijing 100850, P. R. China. E-mail: ruixiao203@sina.com.

† Electronic Supplementary Information (ESI) available: [details of any supplementary information available should be included here]. See DOI: 10.1039/x0xx00000x

Zhang, D. Qin and Y. Xia, *Chem Rev*, 2011, **111**, 3669-3712.
11. L. J. Sherry, S.-H. Chang, G. C. Schatz, R. P. Van Duyne, B. J. Wiley and Y. Xia, *Nano letters*, 2005, **5**, 2034-2038.
12. J. F. Li, Y. F. Huang, Y. Ding, Z. L. Yang, S. B. Li, X. S. Zhou, F. R. Fan, W. Zhang, Z. Y. Zhou, Y. WuDe, B. Ren, Z. L. Wang and Z. Q. Tian, *Nature*, 2010, **464**, 392-395.
13. D.-K. Lim, K.-S. Jeon, J.-H. Hwang, H. Kim, S. Kwon, Y. D. Suh and J.-M. Nam, *Nat Nano*, 2011, **6**, 452-460.
14. A. Lee, G. F. S. Andrade, A. Ahmed, M. L. Souza, N. Coombs, E. Tumarkin, K. Liu, R. Gordon, A. G. Brolo and E. Kumacheva, *Journal of the American Chemical Society*, 2011, **133**, 7563-7570.
15. E. C. Le Ru, E. Blackie, M. Meyer and P. G. Etchegoin, *The Journal of Physical Chemistry C*, 2007, **111**, 13794-13803.
16. N. J. Halas, S. Lal, W. S. Chang, S. Link and P. Nordlander, *Chem Rev*, 2011, **111**, 3913-3961.
17. P.-J. Huang, L.-K. Chau, T.-S. Yang, L.-L. Tay and T.-T. Lin, *Advanced Functional Materials*, 2009, **19**, 242-248.
18. Y. Zhu, S. Murali, W. Cai, X. Li, J. W. Suk, J. R. Potts and R. S. Ruoff, *Advanced Materials*, 2010, **22**, 3906-3924.
19. K. S. Novoselov, V. I. Falko, L. Colombo, P. R. Gellert, M. G. Schwab and K. Kim, *Nature*, 2012, **490**, 192-200.
20. X. Ling, L. Xie, Y. Fang, H. Xu, H. Zhang, J. Kong, M. S. Dresselhaus, J. Zhang and Z. Liu, *Nano letters*, 2010, **10**, 553-561.
21. K. P. Loh, Q. Bao, P. K. Ang and J. Yang, *Journal of Materials Chemistry*, 2010, **20**, 2277-2289.
22. D. R. Dreyer, S. Park, C. W. Bielawski and R. S. Ruoff, *Chem. Soc. Rev.*, 2010, **39**, 228-240.
23. N. Jung, A. C. Crowther, N. Kim, P. Kim and L. Brus, *ACS nano*, 2010, **4**, 7005-7013.
24. L. Xie, X. Ling, Y. Fang, J. Zhang and Z. Liu, *Journal of the American Chemical Society*, 2009, **131**, 9890-9891.
25. X. Ding, L. Kong, J. Wang, F. Fang, D. Li and J. Liu, *ACS applied materials & interfaces*, 2013, **5**, 7072-7078.
26. S. Dutta, C. Ray, S. Sarkar, M. Pradhan, Y. Negishi and T. Pal, *ACS applied materials & interfaces*, 2013, **5**, 8724-8732.
27. D. Lin, T. Qin, Y. Wang, X. Sun and L. Chen, *ACS applied materials & interfaces*, 2014, **6**, 1320-1329.
28. X. Ma, Q. Qu, Y. Zhao, Z. Luo, Y. Zhao, K. W. Ng and Y. Zhao, *Journal of Materials Chemistry B*, 2013, **1**, 6495-6500.
29. L. H. Reddy, J. L. Arias, J. Nicolas and P. Couvreur, *Chemical Reviews*, 2012, **112**, 5818-5878.
30. D. Chen, G. Ji, Y. Ma, J. Y. Lee and J. Lu, *ACS applied materials & interfaces*, 2011, **3**, 3078-3083.
31. M. S. A. Darwish, N. H. A. Nguyen, Š. Alena and I. Stibor, *Journal of Nanomaterials*, 2015, **2015**, 10.
32. W. Yu, Y. Huang, L. Pei, Y. Fan, X. Wang and K. Lai, *Journal of Nanomaterials*, 2014, **2014**, 1-8.
33. K. Kim, H. J. Jang and K. S. Shin, *The Analyst*, 2009, **134**, 308-313.
34. J. Liu, R. Che, H. Chen, F. Zhang, F. Xia, Q. Wu and M. Wang, *Small*, 2012, **8**, 1214-1221.
35. Y. Fang, S. Guo, C. Zhu, Y. Zhai and E. Wang, *Langmuir : the ACS journal of surfaces and colloids*, 2010, **26**, 11277-11282.
36. H. Zhang, D. Hines and D. L. Akins, *Dalton Transactions*, 2014, **43**, 2670-2675.
37. G. Goncalves, P. A. A. P. Marques, C. M. Granadeiro, H. I. S. Nogueira, M. K. Singh and J. Grácio, *Chemistry of Materials*, 2009, **21**, 4796-4802.
38. H. Zhang, Y. Zhao and D. L. Akins, *Journal of Solid State Chemistry*, 2012, **194**, 277-281.
39. H. Zhang, Y. Zhou, Y. Li, T. J. Bandosz and D. L. Akins, *Journal of Colloid and Interface Science*, 2012, **375**, 106-111.
40. J. Polte, M. Herder, R. Erler, S. Rolf, A. Fischer, C. Wurth, A. F. Thunemann, R. Kraehnert and F. Emmerling, *Nanoscale*, 2010, **2**, 2463-2469.
41. T. Wu, H. Shen, L. Sun, B. Cheng, B. Liu and J. Shen, *ACS applied materials & interfaces*, 2012, **4**, 2041-2047.
42. H. Deng, X. Li, Q. Peng, X. Wang, J. Chen and Y. Li, *Angewandte Chemie*, 2005, **117**, 2842-2845.
43. Y. Zhang, B. Chen, L. Zhang, J. Huang, F. Chen, Z. Yang, J. Yao and Z. Zhang, *Nanoscale*, 2011, **3**, 1446-1450.
44. Y.-F. Huang, D.-Y. Wu, H.-P. Zhu, L.-B. Zhao, G.-K. Liu, B. Ren and Z.-Q. Tian, *Physical Chemistry Chemical Physics*, 2012, **14**, 8485-8497.
45. K. Kim, D. Shin, H. B. Lee and K. S. Shin, *Chemical Communications*, 2011, **47**, 2020-2022.
46. A. M. Fales, H. Yuan and T. Vo-Dinh, *The Journal of Physical Chemistry C*, 2014, **118**, 3708-3715.
47. D.-K. Lim, A. Barhoumi, R. G. Wylie, G. Reznor, R. S. Langer and D. S. Kohane, *Nano letters*, 2013, **13**, 4075-4079.
48. G. Wang, G. Chen, Z. Wei, X. Dong and M. Qi, *Materials Chemistry and Physics*, 2013, **141**, 997-1004.